On a slippery slope

Maarten van Reeuwijk[1], Markus Holzner[2], Colm-Cille Caulfield[3] and Harm Jonker[4]

[1] Dept of Civil and Environmental Engineering, Imperial College London, UK
[2]Institute of Environmental Engineering, ETH Zurich, Switzerland
[3]BP Institute and DAMTP, University of Cambridge, UK
[4]Faculty of Geosciences, Delft University of Technology, the Netherlands

Abstract

We explore the physics of turbulent entrainment in inclined gravity currents using Direct Numerical Simulation (DNS). We find that for the case under consideration, entrainment is dominated by outer layer processes, with shear production being responsible for most of the observed entrainment. The entrainment law inferred from the simulation is of the form $E = a(\mathrm{Ri}_{max} - \mathrm{Ri})$ where $a = 0.36$ and $\mathrm{Ri}_{max} = 0.16$, suggesting that there is a maximum value of Ri beyond which turbulence cannot be sustained.

1 Introduction

Gravity currents are a regular occurrence in nature, e.g. katabatic winds, dense downslope releases in the ocean, pyroclastic flows and exchange flows between spaces of differing temperatures. A gravity current exerts a shear on the ambient fluid which consequently leads to turbulence production and mixing, causing ambient fluid to be entrained. Simultaneously, the fluid stratification suppresses mixing, leading to an entrainment relation of the entrainment coefficient E that depends on the Richardson number Ri.

Turbulent entrainment in inclined gravity currents was first studied experimentally by Ellison & Turner (1959). The set-up comprised an inclined channel in which a fluid lighter (heavier) than the ambient was injected which flowed along the channel top (bottom) as a gravity current. By varying the channel inclination angle and thus the bulk Richardson number Ri, an entrainment law of the form $E = f(Ri)$ was observed, which was lateron approximated by $E = (0.08 - 0.1\mathrm{Ri})/(1 + 5\mathrm{Ri})$ (Turner, 1986). However, field campaigns of oceanic overflows and several new experimental investigations have since revealed orders of magnitudes differences in the observed values of E (e.g. Wells *et al.*, 2010), highlighting a need for further understanding of the physical processes responsible for turbulent entrainment.

We perform Direct Numerical Simulation (DNS) of a temporal gravity current on a sloped surface in order to understand the physics of turbulent entrainment. In particular, we capitalise on the recent progress made on entrainment in plumes (van Reeuwijk & Craske, 2015), which allows E to be decomposed into distinct physical processes such as shear production and buoyancy. We use this method to show that the influence of near-wall processes on turbulent entrainment is limited (section 3) for the case under consideration. We then study the entrainment law itself by carrying out simulations at various slope angles in section 4.

2 Case setup

The simulations comprise a temporal version of the classical inclined gravity current experiments of Ellison & Turner (1959); Krug *et al.* (2013). Specifically, the problem entails a negatively buoyant (heavy) fluid layer of infinite extent flowing down a slope of

Table 1: Simulation data. Simulation domain for all simulations is $20h_0 \times 20h_0 \times 10h_0$ at a resolution of $1536^2 \times 1152$. NS, FS: no-slip and free-slip velocity boundary conditions, respectively.

Sim.	α	BC	Re_0	Ri_0	$t_{run}/t^\star$
S2	2	FS	3890	0.50	55
S5	5	FS	3890	0.20	40
S10	10	FS	3890	0.10	40
S10N	10	NS	3890	0.10	40
S25	25	FS	3890	0.04	25
S45	45	FS	3890	0.02	20
S90	90	FS	3890	0.00	20

angle α (van Reeuwijk *et al.*, 2016). The dense fluid layer has an initial buoyancy $b_0 < 0$ and initial velocity U. Here, buoyancy is defined as $b = g(\rho_0 - \rho)/\rho_0$ where g is the gravitational acceleration and ρ_0 is the density of the quiescent layer overhead. For $t > 0$, the flow develops Kelvin-Helmholtz instabilities, after which it transitions to turbulence and flows down the slope as a turbulent gravity current. Because of the problem setup, the flow will remain statistically homogeneous in the x and y direction, and its statistics will thus only depend on the wall-normal coordinate z and time t (see also Fedorovich & Shapiro, 2009). The Reynolds number Re and bulk Richardson number Ri are defined according to

$$\mathrm{Re} = \frac{u_T h_0}{\nu}, \qquad \mathrm{Ri} = -\frac{b_T h \cos\alpha}{u_T^2}, \qquad (1)$$

where u_T, h, and b_T are the characteristic (top-hat) velocity scale, depth and buoyancy, respectively, which can be calculated using (Ellison & Turner, 1959; Krug *et al.*, 2014)

$$u_T h = \int_0^\infty \overline{u}\,\mathrm{d}z, \qquad u_T^2 h = \int_0^\infty \overline{u}^2\,\mathrm{d}z, \qquad b_T h = \int_0^\infty \overline{b}\,\mathrm{d}z. \qquad (2)$$

Here we note that the integral buoyancy forcing $B_0 = -b_T h \sin\alpha = -b_0 h_0 \sin\alpha$ is a conserved quantity in the simulations.

Consistent with the inflow conditions of the experiment of Krug *et al.* (2013), $\mathrm{Re}_0 = U h_0/\nu = 3890$ for all flow cases. The simulations are carried out on a large domain of $20h_0 \times 20h_0 \times 10h_0$ to ensure reliable statistics for this transient problem. A resolution of $N_x \times N_y \times N_z = 1536^2 \times 1152$, sufficient for DNS, is employed for all simulations.

The simulations are carried out with the DNS code SPARKLE, which solves the Navier-Stokes equations in the Boussinesq approximation on a cuboidal domain and is fully parallelized making use of domain decomposition in two directions. The spatial differential operators are discretized using second order symmetry-preserving central differences (Verstappen & Veldman, 2003), and time-integration is carried out with an adaptive second order Adams-Bashforth method (van Reeuwijk *et al.*, 2008). Periodic boundary conditions are applied for the lateral directions. At the top wall, a Neumann (no-flux) boundary condition is imposed for buoyancy and a free-slip boundary condition for velocity. At the bottom wall, a Neumann boundary conditions is used for buoyancy, whilst the velocity boundary conditions are either no-slip (NS) or free-slip (FS).

The simulation details can be found in Table 1. The typical timescale is defined as $t^* = h_0/\sqrt{B_0}$. The simulations were designed such that B_0 was identical for all angles. Simulations typically ran for 72 hours on 1536 cores.

3 Influence of boundary conditions on turbulent entrainment

We first focus on a flow case with $\alpha = 10^o$ and examine the differences between no-slip (simulation S10N) and free-slip (S10) boundary conditions. Clearly, free-slip boundaries do not occur in nature, but if entrainment is dominated by outer layer processes as is often argued, the influence of velocity boundary conditions should be small. The evolution of h and Ri are shown in the top row in Figure 1. The layer thickness h grows slightly faster for S10 than for S10N, indicating higher entrainment in the former. The evolution of Ri in time shows an initial growth to a maximum, after which Ri reduces monotonically and approaches a steady state for $t/t^* > 30$; the final value of Ri is a bit higher for S10N than S10. The approach to a constant value of Ri is qualitatively similar to turbulent plumes, where a "pure" plume will attain a constant value of Ri far away from the source. If the flow has an excess (deficit) of momentum at the source the plume is referred to as forced (lazy) (van Reeuwijk & Craske, 2015; Morton & Middleton, 1973); the flow will adjust itself due to the work done by gravity until it becomes pure. Restricting attention to $t/t_* > 7$ (when the flow has transitioned to turbulence), the gravity current is "lazy", approaching "pure" behaviour for $t/t^* > 30$, say.

The self-similarity of the spatially averaged velocity $\overline{u}$ and buoyancy $\overline{b}$ profiles are shown in the bottom row of Figure 1. Unsurprisingly, the solutions are very different near the wall. The "toe" observed in the buoyancy profile for S10 is caused by the fact that the turbulence production $-\overline{w'u'}\partial\overline{u}/\partial z$ is zero at the velocity maximum and that as a consequence turbulence levels are low. This implies that buoyancy is "trapped" near the wall; an effect reported by Ellison & Turner (1959). Importantly though, the flow profiles in the outer layer are very similar.

The entrainment coefficient E is defined according to

$$E = \frac{1}{u_T}\frac{\mathrm{d}h}{\mathrm{d}t}. \tag{3}$$

The dependence of E on time is shown in the top plot of Figure 2 with red triangles and blue circles for S10N and S10, respectively. The entrainment coefficient E peaks during the violent breakup of the Kelvin-Helmholtz instabilities, and then decays to an approximately constant value for $t/t_* > 20$. Consistent with the observed growth rates of h in Figure 1, E is slightly higher for S10 than S10N.

Using a recently developed framework that allows entrainment to be decomposed into separate physical contributions (van Reeuwijk & Craske, 2015), E can be decomposed as

$$E = E_{\mathrm{prod}} + E_{\mathrm{buoy}} + E_{\mathrm{vis}}. \tag{4}$$

The decomposition, originally developed for entrainment in turbulent jets and plumes, follows from substitution of the definition of h (in terms of the flow integrals) into (3), and substituting the integral momentum and mean kinetic energy equations. The contributions due to shear-production E_{prod}, buoyancy E_{buoy} and viscous effects E_{vis} are given
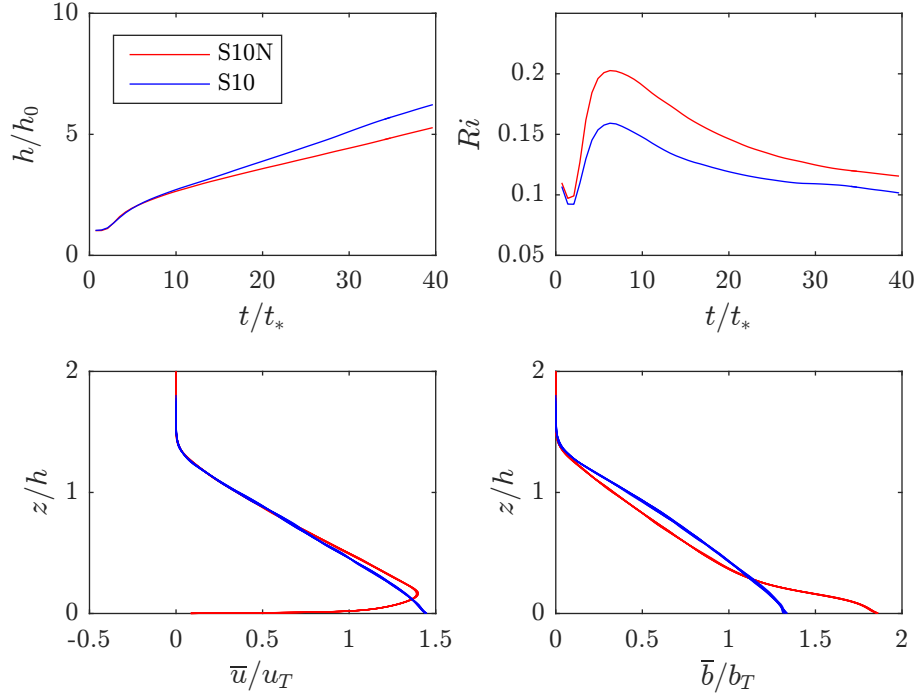
Figure 1: Top row: layer thickness h and bulk Richarson number Ri. Bottom row: self-similarity of $\overline{u}$ and $\overline{b}$.

by

$$E_{\text{prod}} = -\frac{2}{u_T^3} \int_0^\infty \overline{w'u'} \frac{\partial \overline{u}}{\partial z} \mathrm{d}z \tag{5}$$

$$E_{\text{buoy}} = 2\text{Ri} \tan\alpha \left(1 - \frac{1}{u_T b_T h} \int_0^\infty \overline{b}\overline{u} \mathrm{d}z\right) \tag{6}$$

$$E_{\text{vis}} = \frac{2\nu}{u_T^3} \int_0^\infty \left(\frac{\partial \overline{u}}{\partial z}\right)^2 \mathrm{d}z - 2c_f \tag{7}$$

Here, $c_f = \tau_w/u_T^2$ is the friction factor and τ_w is the kinematic wall shear stress.

According to (4), entrainment is determined by three processes. The first is the shear-production term E_{prod}, which will be the dominant source of entrainment in many flows. The second term E_{buoy} represents the influence of buoyancy on turbulent entrainment. The third term E_{vis} represents the viscous effects which are dominant near the wall. The terms contributing to E_{vis} are wall friction, as represented by the friction factor c_f, and the mean dissipation rate integral. The latter will be dominated by the near-wall behaviour, because the integral can be approximated by u_T^2/h in the outer layer, implying that the term is of order Re^{-1}. Thus, at high Re the outer layer contribution is expected to vanish and the integral is only determined by inner layer processes.

The individual terms (5)-(7) are calculated from the flow statistics, and (4) is plotted in the top plot of Figure 2, showing that the decomposition is in excellent agreement with the directly calculated E from (3). The individual terms contributing to E are shown for both flow cases in the bottom row of Figure 2. Quite surprisingly, buoyancy hardly plays a role and all the entrainment is due to turbulence production. As $E_{\text{vis}} < 0$, the viscous contribution acts to lower the entrainment coefficient. This is because τ_w is larger than the mean dissipation integral.
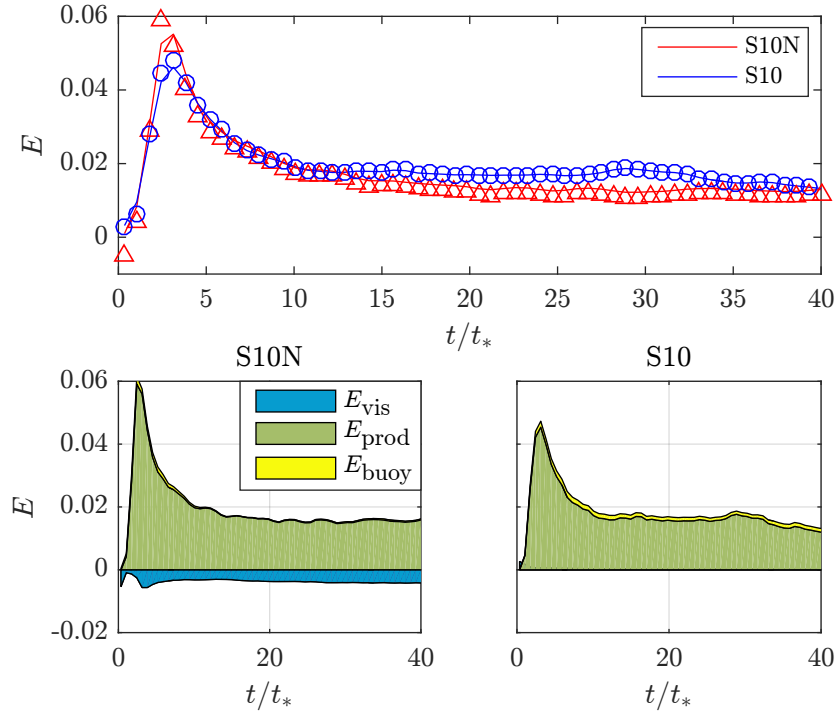
Figure 2: Entrainment decomposition for S10 and S10N. Top: E as a function of time according to its definition (3) (symbols) and via the decomposition (4) (lines). Bottom: the individual terms comprising E for both simulations.

4 The entrainment law

Having established that the boundary conditions have limited influence on turbulent entrainment, we restrict attention to free-slip velocity boundary conditions in order to focus on outer layer dynamics only and vary the angle α between 2 and 90 degrees, the 90^0 case closely resembling a temporal plume (and thus strictly a different flow). The evolution of E is shown for all simulations in the top plot of Figure 3. Clearly, E has higher values at larger angles α and since α is directly related to the bulk Richardson number Ri, this points to a dependence of E on Ri. Despite keeping B_0 the same for all simulations, the smallest angles are challenging since lower turbulence levels will be low as a result of the stronger stratification (not shown). This is particularly evident in S2, in which the flow nearly relaminarises after the initial burst of turbulence associated with the Kelvin-Helmholtz instabilities. However, the near absence of turbulence implies that the fluid layer will accelerate until a second transition occurs after which the coveted "pure" behaviour emerges for $t/t_* > 50$.

The entrainment law $E(\mathrm{Ri})$ is shown in the bottom plot of Figure 3, together with the Ellison and Turner entrainment law (ET59) which was provided in the introduction. Here, Ri is the value associated with the "pure" gravity current. Clearly, Ri remains constrained between $0 < \mathrm{Ri} < 0.2$ for all angles, and it is impossible to reach the higher values of Ri observed in the Ellison & Turner (1959) experiments. Furthermore, the values of E are significantly lower. Although it is clear that the spatial case is different from the temporal case considered here, it is conceivable that the gravity current in the Ellison and Turner experiments was not yet "pure", which would go some way in explaining higher values for Ri and E.

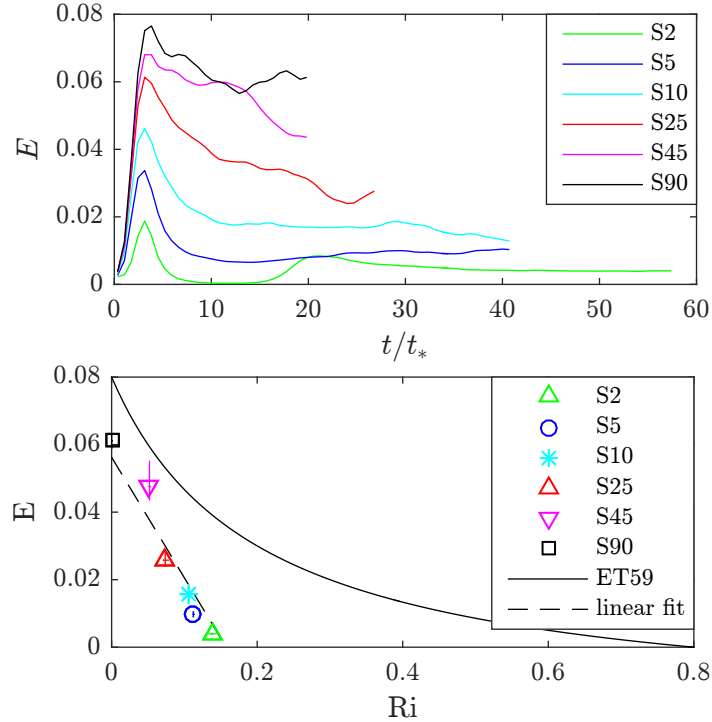The entrainment law can be reasonably well approximated by a relation of the form

Figure 3: Entrainment rate. Top: plotted as a function of time for various α. Bottom: plotted as a function of Ri.

$E = a(\mathrm{Ri}_{\max} - \mathrm{Ri})$ where $a = 0.36$ and $\mathrm{Ri}_{\max} = 0.16$, as indicated in the bottom row of Figure 3 by the dashed line. This suggests that there is a maximum value of Ri beyond which turbulence cannot be sustained. This is close to the well-known Miles-Howard criterion for linear normal mode stability of inviscid parallel steady stratified shear flows and consistent with observations of Ri close to 1/4 in the equatorial undercurrent (Smyth & Moum, 2013). Therefore, a possible explanation is that shear instability is being strongly suppressed as Ri increases towards these values. An alternative possible interpretation, consistent with classical Monin-Obukhov similarity for wall-bounded stratified turbulent flow and as recently demonstrated by Zhou *et al.* (2016) through simulation of stratified plane Couette flow, is that such wall-bounded stratified flows adjust so that Ri cannot take values substantially greater than 0.2. The simulations presented here constitute further evidence that such throttling of strongly stratified shear flows may well be a generic property, although much further research is required to distinguish between whether this throttling is associated with the transitionary properties of the developing instabilities, or the quasi-stationary properties of the developed turbulence.

5   Conclusions

The temporal gravity current is a canonical stratified turbulence problem that has turbulent entrainment as one of its core features. We showed that the bottom velocity boundary condition has little influence on the entrainment coefficient E for this flow problem. By applying a new method for decomposing E into various different contributions, originally developed for entrainment in turbulent jets and plumes, we show that the entrainment is predominantly due to shear-production. The effect of buoyancy on E is surprisingly small; clearly buoyancy does not directly affect entrainment, although it will have a significant indirect influence via its effect on the turbulence (which in turn influences the

shear production).

The DNS simulations reveal an entrainment law which decreases linearly in Ri, with the fit crossing the abscissa at $\mathrm{Ri}_{\max} = 0.16$, thus implying that there exists an upper value of Ri beyond which turbulence cannot be sustained.

References

ELLISON, T. H. & TURNER, J. S. 1959 Turbulent entrainment in stratified flows. *J. Fluid Mech.* **6**, 423–448.

FEDOROVICH, E. & SHAPIRO, A. 2009 Structure of numerically simulated katabatic and anabatic flows along steep slopes. *Acta Geophysica* **57** (4), 981–1010.

KRUG, D., HOLZNER, M., LÜTHI, B., WOLF, M., KINZELBACH, W. & TSINOBER, A. 2013 Experimental study of entrainment and interface dynamics in a gravity current. *Exp. Fluids* **54**, 1530.

KRUG, D., HOLZNER, M., LÜTHI, B., WOLF, M., TSINOBER, A. & KINZELBACH, W. 2014 A combined scanning PTV/LIF technique to simultaneously measure the full velocity gradient tensor and the 3D density field. *Measurement Science and Technology* **25** (6), 065301.

MORTON, B. R. & MIDDLETON, J. 1973 Scale diagrams for forced plumes. *J. Fluid Mech.* **58**, 165–176.

VAN REEUWIJK, M. & CRASKE, J. 2015 Energy-consistent entrainment relations for jets and plumes. *J. Fluid. Mech.* **782**, 333—355.

VAN REEUWIJK, M., JONKER, H. J. J. & HANJALIĆ, K. 2008 Wind and boundary layers in Rayleigh-Bénard convection. i. analysis and modelling. *Phys. Rev. E* **77**, 036311.

VAN REEUWIJK, M., KRUG, D. & HOLZNER, M. 2016 Small-scale entrainment in gravity currents. *Env. Fluid Mech* **under review**.

SMYTH, W. D. & MOUM, J. N. 2013 Marginal instability and deep cycle turbulence in the eastern equatorial pacific occean. *Geophys. Res. Lett.* **40**, 6181–6185.

TURNER, J. S. 1986 Turbulent entrainment: the development of the entrainment assumption, and its application to geophysical flows. *J. Fluid Mech.* **173**, 431–471.

VERSTAPPEN, R. W. C. P. & VELDMAN, A. E. P. 2003 Symmetry-preserving discretization of turbulent flow. *J. Comput. Phys.* **187** (1), 343–368.

WELLS, M., CENEDESE, C. & CAULFIELD, C. P. 2010 The relationship between flux coefficient and entrainment ratio in density currents. *Journal of Physical Oceanography* **40** (12), 2713–2727.

ZHOU, Q., TAYLOR, J. R. & CAULFIELD, .C. P. 2016 Self-similar mixing in stratified plane couette flow for varying prandtl number. *J. Fluid Mech* **submitted**.